Article

Suppression of Vortex-Induced Vibration and Phase-Averaged Analysis of the Wake Generated by a Circular Cylinder Covered with Helical Grooves

Zhiyong Hao [1], Chenlin Sun [2], Yucen Lu [3], Kaiming Bi [4] and Tongming Zhou [2,*]

[1] College of Logistics Engineering, Shanghai Maritime University, Shanghai 201306, China; haozhiyong@shmtu.edu.cn

[2] Department of Civil and Resource Engineering, The University of Western Australia, 35 Stirling Highway, Crawley, WA 6009, Australia; chenlin.sun@research.uwa.edu.au

[3] Aurecon Group, Level 5, 116 Military Road, Neutral Bay, Sydney, NSW 2089, Australia; yucenlu@gmail.com

[4] Centre for Infrastructure Monitoring and Protection, School of Civil and Mechanical Engineering, Curtin University, Kent Street, Bentley, WA 6102, Australia; kaiming.bi@curtin.edu.au

* Correspondence: tongming.zhou@uwa.edu.au

Abstract: The effect of triple helical grooves on the suppression of vortex-induced vibration (VIV) of a circular cylinder was investigated experimentally in a wind tunnel over Reynolds number in the range of $1 \times 10^4 < Re < 4 \times 10^4$. It was found that the helical grooves were effective in suppressing VIV with the peak amplitude reduction of approximately 36%. In addition, the lock-on region was also reduced. To explore the mechanism for the suppression of VIV, experiments on flow structures for a stationary grooved cylinder were also conducted in a wind tunnel at a free stream velocity U_∞ of 4.37 m/s, corresponding to a Reynolds number based on the bare cylinder diameter of about 3500. The data were then analyzed using the phase-averaged method to evaluate the coherent vortex structures in the wakes. The results for the stationary grooved cylinder showed that the grooves weakened vortex shedding in the near wake. In addition, the grooves also reduced the drag coefficient by 6.6%. These results help explain the reduction of VIV using helical grooves.

Keywords: helical grooves; vortex-induced vibration; passive control; circular cylinder wake

1. Introduction

Vortex-induced vibration (VIV) is a phenomenon arising due to fluid-structure interaction and may cause structural failure due to the large amplitude of the vibration. Understanding the vorticity field and the mechanism of the vortex shedding behind bluff bodies is crucial for the effective suppression of VIV. In the past decades, numerous investigations have been conducted to understand the flow around a circular cylinder. Though simple in cross-sectional geometry, the flow around a circular cylinder contains complex interaction of shear layers, namely, boundary layer, free shear layers, and the wake of the cylinder. The boundary layer separation over the surface of a cylinder leads to the alternating von Kármán vortex street. These vortices further induce time-dependent dynamic loads on the cylinder surface, and may cause both transverse and longitudinal vibrations of the cylinder if the vortex shedding frequency matches the structural frequency [1]. This is known as vortex-induced vibration. The vibration of the cylinder normally persists over a range of flow velocity, or Reynolds number Re, which is defined as $Re = U_\infty d/\nu$ with U_∞ being the free stream velocity, d the diameter of the cylinder, and ν the kinematic viscosity of the fluid. This range is also called the lock-on region. It is widely recognized that VIV can cause fatigue failure of the structures and therefore a lot of methods have been proposed to suppress vortex shedding and, hence, VIV, using both experimental and numerical methods [2]. There are two ways to suppress VIV, namely, active and passive methods, depending on whether external energy needed or only passive modifications of

the geometry of the bluff structures. One of the advantages of the active method is that the control system can sense the current flow-structure circumstances and adapt to the real-time updated environmental conditions to mitigate the vibrations of the structure [3]. However, the continuous external energy supply and the complex feedback system make the active method costly and impractical to use in most industrial applications. For its manageable implementations and operations, the passive approaches have been widely investigated and employed for practical purposes, including helical strakes, fairings and splitter plates, cactus-inspired shapes, etc. As reviewed by Wang and Lin [4], while the fairings and splitter plates can both suppress VIV and reduce the drag, the helical strakes reduce the VIV amplitude with the cost of the increased drag coefficient. It should be noted, however, that fairings and splitter plates may cause galloping with unwanted large amplitudes of VIV under certain conditions. Therefore, the design of the passive devices as well as the underlying VIV suppression mechanism should be carefully studied before the engineering application. For offshore and wind engineering applications, helical strakes are the most common and widely used passive device [4,5]. As revealed by Zhou et al. [6] and Huang [7], the helical configuration can prevent the correlation of vortex shedding along the spanwise direction and, therefore, the VIV suppression is independent of the oncoming flow direction. Ishihara and Li [8] conducted the numerical simulations on VIV suppression of a circular cylinder by helical wires for a large mass ratio of 248 and a small damping ratio of 0.00257 over a range of Reynolds numbers $16{,}000 \leq Re \leq 24{,}500$. The numerical study found that the helical wires with a diameter of $0.1d$ effectively suppress the amplitude of VIV by nearly 80% and avoid the "lock-on". It is also found that the fluctuating lift forces and their spanwise correlation for the wired cylinder are significantly reduced comparing with those for the bare cylinder, due to the enhancement of three-dimensional disturbance to the wake caused by helical wires. Since the objective of studies on VIV is the understanding, prediction, and prevention of VIV preferably without drag penalty, it is necessary to develop an alternative helical design from a practical aspect [6,9].

Like helical strakes, the suppression mechanism of helical grooves can be expected in two aspects: firstly, the grooves may destroy or suppress the interaction between two shear layers, and secondly, grooves prevent the vortices from becoming correlated in the spanwise direction. Huang [7] proposed that, instead of adding devices which protrude outwards around the buoyancy modules of the deep-water marine risers and, hence, definitely cause a significant increase in drag coefficient, it is possible to fabricate grooves to the riser modules. Huang [7] carried out experimental investigations to examine the effects of triple-starting helical grooves on the drag of a fixed circular cylinder and the vortex-induced vibration of an elastically supported cylinder. For the elastically supported cylinder, the Reynolds number varied over a range of 13,000–46,000, while for the fixed cylinder, it was in the range of 31,000–375,000. It was found that the helical grooves were effective in suppressing the vortex-induced cross-flow vibration amplitudes with the peak amplitude being reduced by 64% compared with that of the smooth cylinder. Drag reductions of up to 25% were also achieved in the sub-critical Reynolds number range tested for the fixed cylinders. The grooves also eliminated the "drag crisis" region. Zhou et al. [10] investigated the flow around a smooth cylinder and a rough cylinder with rectangular-shaped grooves oriented in the longitudinal direction at various Reynolds numbers in the subcritical regime ($7430 \leq Re \leq 17{,}980$). The flow fields in the near wake were measured using PIV technique. It was found that the grooved surface is effective in modifying the near-wake flow structure behind the cylinder. The ensemble-averaged flow fields clearly show that the wake of the grooved cylinder is both more compact (in streamwise direction) and narrower (in transverse direction) than that of the smooth cylinder at the same Reynolds number (with the length of recirculation zone decreased by about 15–25%), together with reduced magnitude of the turbulent kinetic energy, Reynolds shear, and normal stresses. This is in accordance with the force measurement results that the grooved cylinder demonstrates a significant reduction of the mean drag coefficient by about 18–28%, as compared to the smooth cylinder at the same Reynolds number. Law and Jaiman [9]

conducted a numerical study on the effect of spanwise grooves on the VIV suppression and the reduction of drag force. They proposed a novel staggered groove configuration, whose geometry was especially designed by offsetting the cross-sectional portion of the cylinder continuously along the spanwise direction. The authors assessed the VIV responses of the proposed staggered groove configuration against the helical grooves. The staggered and helical groove configurations differed only in the arrangement of cross-section geometry along the spanwise direction. Three-dimensional coupled fluid–structure simulations were conducted at low mass and damping values with a moderate Reynolds number of $Re = 4800$. The numerical results showed that the staggered groove configuration is effective in suppressing VIV, wherein the net reductions of 37% in the peak transverse amplitude and about 25% in the mean drag coefficient were observed in comparison to the plain cylinder counterpart. To understand the three-dimensional flow characteristics of near-wake, Law and Jaiman [9] also examined the force cross-correlations for both lift and drag coefficients along the spanwise direction. They found that both the helical grooved cylinder and the plain cylinder had similar frequency spectra of sectional lift and drag coefficients along the spanwise direction, indicating the coherent vortex patterns induced in the wake region. However, the frequency spectra of the staggered grooves have a larger variation along the spanwise direction, leading to both lower amplitudes and the hydrodynamic forces on the vibrating system. The three-dimensional instantaneous iso-surface of vorticity further confirms their findings.

So far, there is a lack of systematic study on the dynamics and evolution of the vortex structures in the wake of a circular cylinder with helical grooves. The experimental investigations on the coherent and incoherent contributions to the time-averaged velocity and Reynolds stresses in the downstream region are barely reported. Thus, this study aims to investigate the effectiveness of helical grooves on vortex shedding and VIV suppression of a grooved cylinder with a pitch length of 7.5d, a width of 0.19d, and a depth of 0.12d. The phase-averaged velocities, vorticity, and contribution to Reynolds stresses at different downstream locations of the wake are examined by comparing with that of a bare circular cylinder wake. The results presented in this study should gain some new insight into the wake vortex dynamics and serve to a better understand of the underlying physics for VIV suppression using helical grooves.

2. Experimental Setup

Measurements of the cross-flow vibration of both the bare and the grooved cylinders were conducted over a range of Reynolds numbers $1 \times 10^4 < Re < 4 \times 10^4$ in the closed-circuit wind tunnel with a test section of 1300 mm (width) × 1800 mm (height) to quantify the effectiveness of helical grooves on the suppression of VIV. The cylinders have an external diameter d of 60 mm and a length of 1290 mm. The aspect ratio L/d for both cylinders is 20. The grooved cylinder was fabricated by adhering lengths of EPDM (Ethylene Propylene Diene Monomer) rubber tape around a bare cylinder, resulting in a diameter d of 80 mm. The grooves had a pith length of 7.5d, a width of 0.19d, and a depth of 0.12d. The mass of the bare cylinder was 1.84 kg and the mass of the cylinder with grooves was 1.96 kg. The test cylinders were flexibly mounted to a steel frame by four identical steel springs to suspend the cylinder approximately 900 mm off the wind tunnel floor. The springs were selected based on their stiffness and length. They must be stiff enough and long enough to remain in tension when measuring the amplitude of vibrations. The four springs were made of steel and had a stiffness of 1680 N/m with an original length of 260 mm. The stiffness was measured by applying a known load to the springs and measuring the subsequent deflection. Once the springs were attached to the cylinder, the top and bottom springs were extended to a length of approximately 325 mm to ensure the system was in tension throughout testing. The experimental setup for cylinder VIV is illustrated in Figure 1.
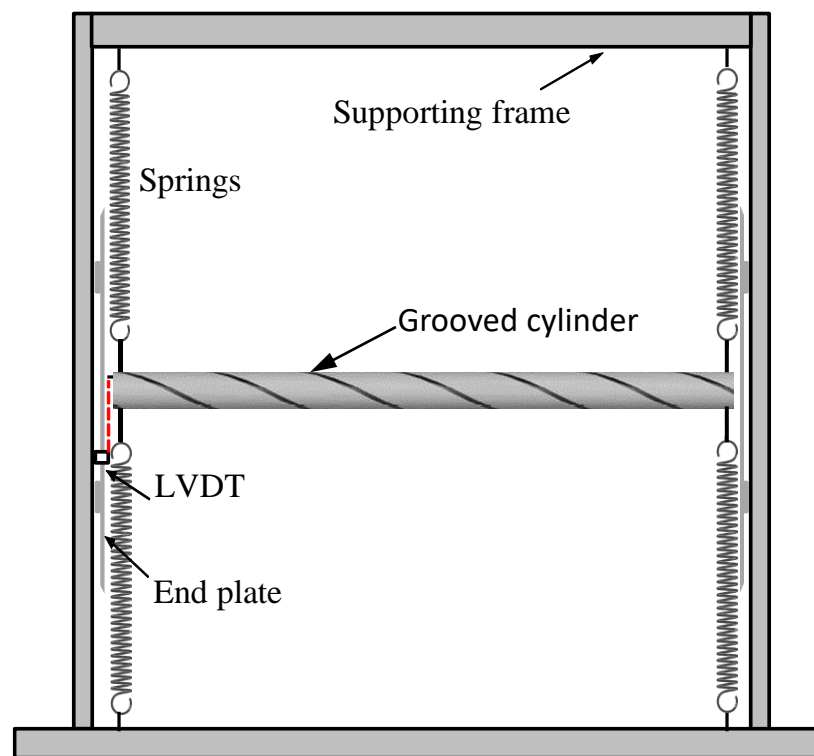
Figure 1. Sketch of the experimental setup for VIV response of the elastically supported cylinders.

The amplitude of the vibrations was measured using a Linear Variable Differential Transformer (LVDT) laser. The laser was cantilevered from the frame's vertical member approximately 190 mm below a white card fixed to the bottom of the cylinder and had a range of ±110 mm. The vibration of the cylinder was digitized into a computer at an interval of 3 ms for about 3 min. The natural frequencies f_n of the bare cylinder and the grooved cylinder (7.87 Hz and 8.06 Hz, respectively) are obtained from the free decay tests. More details of the VIV experiments can be found in Sun et al. [11].

For the purpose of examining the spanwise cross-correlations, two X-wire probes located at $x/d = 10$ and $y/d = 0.5$ were used with one probe fixed and the other moving along the cylinder length direction. The separation between the two probes was in the range of 30–460 mm with an increment of 10 mm for each measurement. The hot-wires were operated with in-house constant temperature circuits at an overheat ratio of 1.5. Each of the two wires in the X-wire probe had a diameter of 5 μm. The wire separation was about 1 mm. The output signals from the anemometers were low-pass filtered through the buck and gain circuits at a cut-off frequency $f_c = 2800$ Hz, depending on the measurement location and free stream velocity. In the present study, the sampling frequency is 5600 Hz.

To further investigate the wake characteristics of the cylinders and the mechanism of VIV suppression of the grooved cylinder, fixed cylinder tests were undertaken in an open-circuit wind tunnel with a test section of 380 mm (width) $\times$ 255 mm (height) and 1.8 m (length). The freestream velocity in the test section was uniform to 0.1%, and the longitudinal turbulence intensity was less than 0.2%. Experiments were conducted in the wakes of both a bare cylinder and a helically grooved cylinder. Both cylinders have an external diameter d of approximately 12 mm and a length of 380 mm. The aspect ratio of both cylinders is $L/d = 32$. The bare cylinder is used as a basis for comparison with the grooved cylinder. The triple helical grooves have a pitch length of $7.5d$, a width of $0.2d$, and a depth of $0.12d$, which are the same as that used for VIV tests. All measurements were performed at a free stream velocity U_∞ of 4.37 m/s, corresponding to a Reynolds number based on the bare cylinder diameter of about 3500, and at streamwise locations of $x^* = 10$, 20, and 40. Hereafter, a superscript asterisk denotes normalization by cylinder

diameter and/or free stream velocity. Boundary layer flows at $x^* = 40$ were also measured both before and after the models were inserted in the wind tunnel to make sure that at this streamwise location, the wake flows were not influenced by the tunnel boundaries. To examine the streamwise evolution of the wakes, an X-type hot-wire probe was moved across the wake in the y-direction to measure the longitudinal and transverse velocity components, u and v, respectively. Another X-probe located at $y^* = 1\sim2$ from the wake centerline was fixed at the wake edge to provide a phase reference to the measured velocity signals for conducting the phase-averaged analysis of the coherent structures in the wakes. The separation between the two wires of the X-probe was about 1.0 mm. The hot-wires were etched to a length of 1 mm from Wollaston (Pt−10% Rh) wires of 5 μm in diameter. Angle calibration was performed over $\pm20°$. The hot-wires were operated with in-house constant temperature circuits at an overheat ratio of 1.5. The output signals were low-pass filtered at a frequency f_c of 2800 Hz. The filtered signals were sampled at a frequency f_s of 5600 Hz into a computer using a 16-bit A/D converter (National Instrument). The sampling period T_s was 45 s. Experimental uncertainties were inferred from the errors in hot-wire calibration as well as the scatter observed in repeating the experiments several times. The uncertainty for the time-averaged velocity, $\overline{U}$, was estimated to be about $\pm2\%$, while for the root-mean-square (rms) values of the fluctuating velocities u and v and the Reynolds shear stress $\langle uv \rangle$, the uncertainties were about $\pm5\%$, $\pm6\%$ and $\pm8\%$, respectively. The tests and flow conditions are summarized in Table 1.

Table 1. Summary of the experimental setup.

Main Particulars	VIV Tests	Fixed Cylinder Tests
Wind tunnel type	closed-circuit	open-circuit
Cylinder diameter (mm)	60	12
Cylinder aspect ratio (L/d)	20	32
Groove dimensions (length × width × depth, mm)	$7.5d \times 0.19d \times 0.12d$	$7.5d \times 0.2d \times 0.12d$
Reynolds number ($U_\infty d/\nu$)	$1 \times 10^4 < Re < 4 \times 10^4$	3500
X-wire probes locations (x/d)	10	10, 20, 40

3. Phase and Structural Averaging

At a certain range of flow velocities or Reynolds numbers, the periodic detachment of pairs of alternate vortices from a bluff body forms an oscillating wake, namely, the von Kármán vortex street, behind the cylinder leading to the fluctuating forces to be experienced by the cylinder. The repeating pattern of swirling vortices and the regular vortex motion are highly periodic. In order to capture and understand the properties of this periodicity and pattern of vortex dynamics, a phase-averaged technique can be used. The phase-averaging, triple decomposition, and structural averaging have been discussed in detail previously [12–16]. Briefly, following Zhou et al. [16], the Q-signal (e.g., the velocity signal measured by a movable hot-wire probe) and Q_R-signal (e.g., a reference signal measured by a reference probe) were both digitally band-pass filtered with a central frequency of the Kármán vortex shedding frequency, f_0. The two phases of particular interest were identified on the filtered signal Q_f, viz.

$$\text{Phase A}: \ Q_f = 0 \text{ and } \frac{dQ_f}{dt} > 0 \tag{1}$$

$$\text{Phase B}: \ Q_f = 0 \text{ and } \frac{dQ_f}{dt} < 0 \tag{2}$$

The two phases correspond to time $t_{A,i}$ and $t_{B,i}$ (measured from an arbitrary time origin), respectively, in Figure 2. The phase Φ was then calculated from Q_f, viz.

$$\phi = \pi \frac{t - t_{A,i}}{t_{B,i} - t_{A,i}}, \ t_{A,i} \leq t \leq t_{B,i} \tag{3}$$
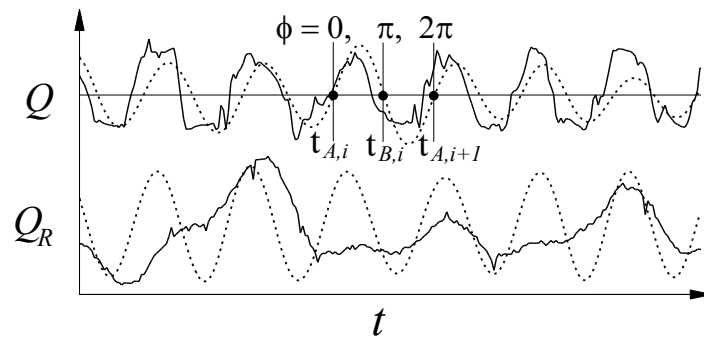
Figure 2. Typical examples of signal Q (**top**) and the reference signal Q_R (**bottom**). The solid and dotted lines represent the original and filtered signals, Q_f, respectively.

The interval between phases A and B was made equal to $0.5/f_0$ by compression or stretching; it was further divided into 30 equal intervals. The difference between the local phase at each y-location of the vorticity probe and the reference phase of the fixed X-wire was used to produce phase-averaged sectional streamlines and contours of coherent and incoherent vorticities in the (Φ, y)-plane. The phase-average of an instantaneous quantity Q is given by

$$< Q >_j = \frac{1}{N} \sum_{i=1}^{N} Q_{j,i} \tag{4}$$

where N is the total number of available cycles and j represents different phases. For convenience, the subscript j will be omitted hereinafter. In the present study, a total of 1800 periods are used for phase averaging in Equation (4). Using a triple decomposition [17], the variable Q can be written as the sum of a time-averaged component $\overline{Q}$, a coherent fluctuation $\widetilde{q}$, and a remainder q_r, viz.

$$Q = \overline{Q} + \widetilde{q} + q_r \tag{5}$$

where Q stands for instantaneous vorticity and the fluctuation q is given by

$$q = \widetilde{q} + q_r \tag{6}$$

The coherent fluctuation $\widetilde{q}$ ($\equiv < q >$) reflects the effect from the large-scale coherent structures while the remainder q_r includes the incoherent structures. The phase-average of the global Reynolds stresses, qs, can be obtained,

$$< qs > = \widetilde{q}\widetilde{s} + < q_r s_r > \tag{7}$$

where q and s can stand for either u or v. Once the coherent components of the q and s fluctuations are extracted using the phase averaging technique, the coherent contributions to the Reynolds stresses or vorticity variance can be estimated in terms of the structural average. The phase-averaged structure begins at k_1 samples before the detection instant and ends at k_2 samples after this instant. The structural average, denoted by a double over bar, is defined by

$$\overline{\overline{\widetilde{q}\widetilde{s}}} = \frac{1}{k1 + k2 + 1} \sum_{-k1}^{k2} \widetilde{q}\widetilde{s} \tag{8}$$

4. Results and Discussion

4.1. Vortex-Induced Vibration for the Bare and Grooved Cylinders

In order to validate the current experimental setup, the dynamic response of a single bare cylinder is tested first. The response of the cylinder can be described in terms of the vibration amplitude A/d versus the reduced velocity V_r, which is defined as $V_r = U_\infty/f_n d$. It was found that for each reduced velocity, the vibration increases for a period of approx-

imately 100 s before it stabilizes at the maximum vibration amplitude, after which the amplitude of vibration does not change. A test of about 120 s was recorded after stable patterns of vibrations were observed. The amplitudes of vibration were determined by averaging the 10% highest peaks recorded on the time history of the displacement after the vibration becomes stable [10,18,19]. The vibration responses at different reduced velocities were compiled and displayed in Figure 3 for the cylinders in the present study. It can be seen that the maximum peak amplitude is about 0.62, occurring at a reduced velocity of about 6.5, which is within the consensus range found in the literature that the lock-on region occurs over V_r = 5–10 [1,20]. The present results for both bare and grooved cylinders are also compared with the results by Huang [7] in which the elastically supported cylinders were attached to a vertically cantilevered supporting rod and towed in a towing tank. Both the in-line and cross-flow vibrations were permitted in Huang [7] over a range of Reynolds numbers 13,000 $\leq$ Re $\leq$ 46,000. For the bare cylinder, there is a distinct amplitude peak for both the present and Huang [7]. For the grooved cylinder, while there is no distinct peak in Huang [7], but replaced by a plateau, the present results show a peak amplitude of about 0.41, occurring around V_r = 5.8. The lock-on region is reduced to V_r = 5–8. Therefore, the present results show that the helical grooves were effective at suppressing VIV with the peak amplitude reduction of approximately 36%.
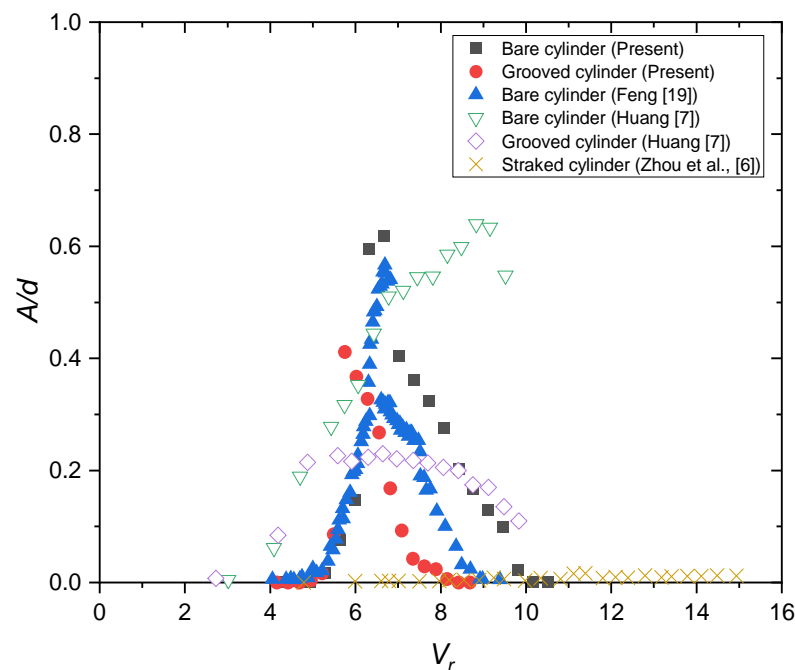
Figure 3. VIV response for both bare and grooved cylinders [6,7,19].

4.2. Vortex Shedding Frequency

Spectral analysis is conducted to determine the vortex shedding frequency based on the transverse velocity components measured by an X-type hot-wire probe using Fast Fourier Transforms (FFT). Figure 4 shows the spectra for both bare cylinder and grooved cylinder wakes measured at y^* = 1 for different streamwise locations, where the frequency is normalized as $f^* = fD/U_\infty$, and the peak frequency corresponds to the Strouhal number. For the convenience of comparing the results, the spectra have been shifted down by a factor of 10 compared with the last location. It can be seen that vortex shedding at each downstream location is apparent at a singular frequency indicated by a sharp peak. This peak frequency corresponds to f^* = 0.21 for the bare cylinder and 0.20 for the grooved cylinder. Both values agree well with the consensus results reported in the literature, indicating that vortex shedding still exists in the wake of the helically grooved cylinder. This result is apparently different from that for the straked cylinder wakes [6], where it was

shown that vortex shedding had been suppressed successfully by the helical strakes, as shown in Figure 4. The peak heights decrease quickly as evolving downstream, indicating the decay of the vortices. At the downstream location of $x^* = 40$ the peak height, relative to its plateau, is far less noticeable, indicating that at this location, the vortices have nearly decayed completely. When comparing the peak energy of the cylinders at the downstream location of $x^* = 10$, the bare cylinder displays a 5% higher peak energy response than that of the grooved one, indicating that the grooves may disrupt the intensity of vortices.
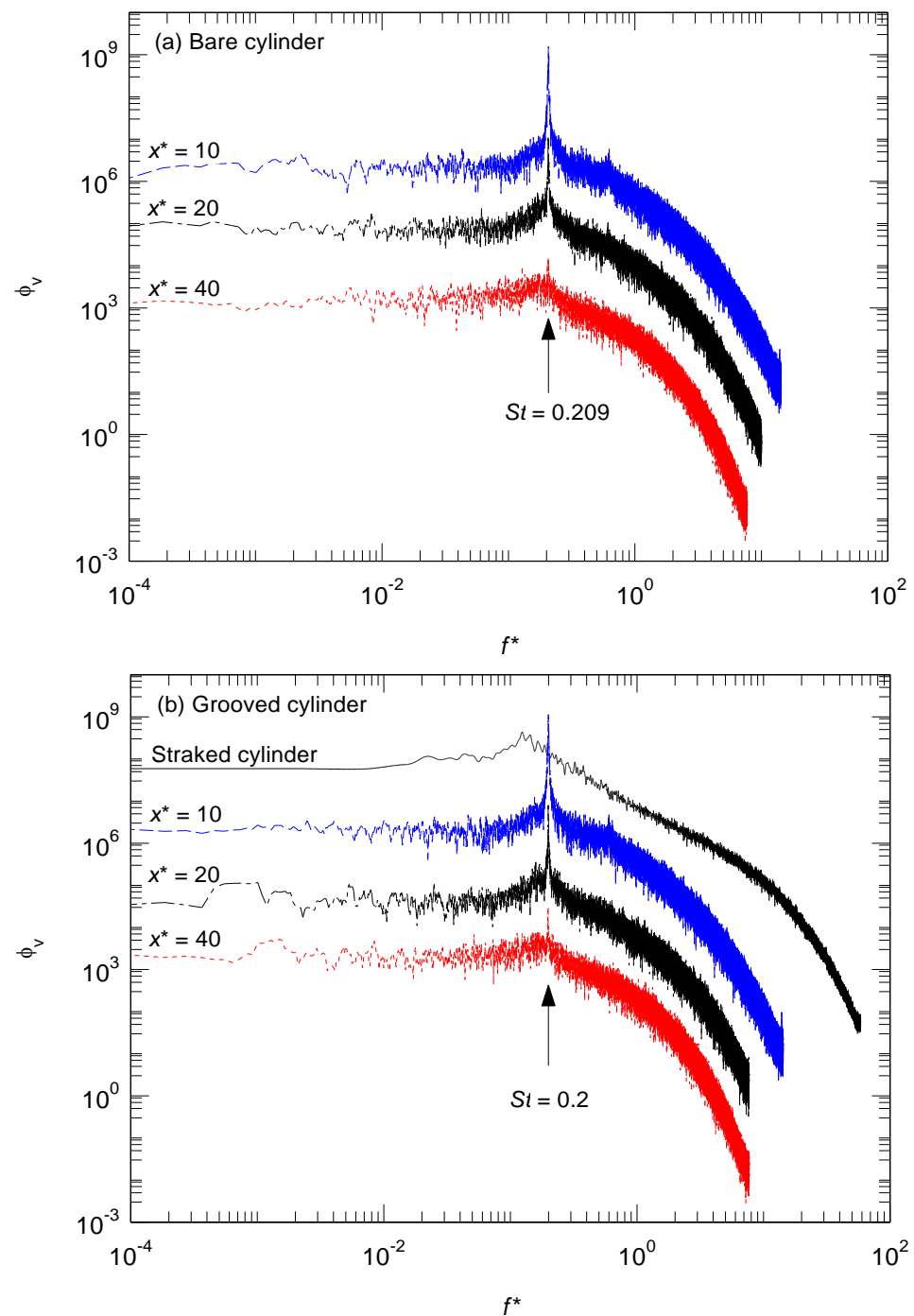
Figure 4. Energy spectra Φ in the wake at $y^* = 1$ for different streamwise locations. (**a**) bare cylinder; (**b**) grooved cylinder. The spectrum for the straked cylinder is from [6] measured at $x^* = 5$ for $Re = 20,430$.

4.3. Cross-Correlations and Drag Coefficients of the Stationary Cylinder Wakes

In turbulent wakes, vortices are shed in cells whose averaged length scale is normally termed as the correlation length [1]. It can be quantified by the spanwise cross-correlation coefficients of two velocity signals, as defined below:

$$\rho_{\alpha_1,\alpha_2}(\Delta z) = \frac{< \alpha_1(z)\alpha_2(z + \Delta z) >}{\sigma_{\alpha_1}\sigma_{\alpha_2}} \tag{9}$$

where α_1 and α_2 represent the velocity component u or v at two points separated in the spanwise direction of the cylinder by a distance Δz, and σ represents standard deviations of α_1 and α_2. The correlation length is then calculated using the following integral [21]:

$$L_{\alpha_1,\alpha_2} = \int_0^{L_0} \rho_{\alpha_1,\alpha_2}(\Delta z)dz, \tag{10}$$

where the integration upper limit L_0 is at the location where the cross-correlation coefficient first becomes zero.

The cross-correlation coefficients between v_1 and v_2 measured at $x^* = 10$ and $Re = 19{,}000$ are shown in Figure 5. It can be seen that all the cross-correlation coefficients decrease with the increase of probe separation, especially at small separations. The magnitude of $\rho_{v_1,v_2}(\Delta z)$ in the bare cylinder wake is much larger than that in the grooved cylinder wake, indicating larger vortical structures for the former than the latter at this downstream location. The correlation length L_{v_1,v_2} evaluated using Equation (10) of the bare cylinder wake is 0.35d, which is about 30% higher than that of the grooved cylinder wake ($L_{v_1,v_2} = 0.27d$). This result suggests that the helical grooves have successfully disrupted the vortical structures in the spanwise direction and thus enhancing the three-dimensionality of the flow. It is in agreement with that proposed by Bearman and Branković [22], who suggested that the strakes do not necessarily suppress vortex shedding, but they prevent the shedding from becoming correlated along the span. The above values of the correlation length of the two wakes are much smaller than those obtained at $x^* = 5$ for bare and the straked cylinders [6], indicating the quick decay of the vortical structures.
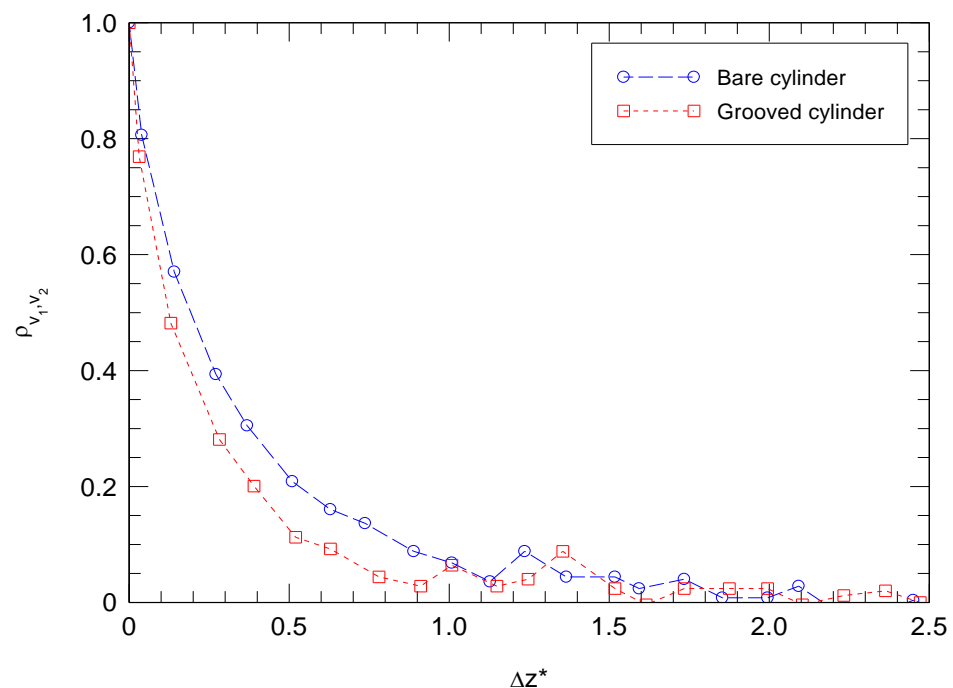
Figure 5. Cross-correlation coefficients of the transverse velocity components for the bare and grooved cylinder wakes obtained at $x^* = 10$ for $Re = 19{,}000$.

It is expected that helical grooves should modify the flow in the boundary layer, thus affecting the vorticity dynamics and force coefficients of the cylinder. Previous studies have shown that vortex suppression can be associated with drag reduction as strong vortex shedding can cause increased steady drag on a structure [23]. The drag coefficient of the cylinders was calculated using the method proposed by Antonia and Rajagopalan [24], via

$$C_d = 2 \int_{-\infty}^{\infty} \frac{U}{U_\infty} \left(\frac{U_\infty - U}{U_\infty} \right) d(y^*) + 2 \int_{-\infty}^{\infty} \left(\frac{v'^2 - u'^2}{U_\infty^2} \right) d(y^*) = I_1 + I_2 \qquad (11)$$

The above integral I_1 is the drag contribution due to momentum thickness while I_2 is the contribution due to Reynolds stresses. Table 2 lists the drag coefficients and the contributions I_1 and I_2 for both cylinders at various downstream locations. The drag coefficient for the bare cylinder is consistent with previous studies for cross flow in sub-critical flow regimes [22]. The contribution from Reynolds stresses is more substantial in the near wake region ($x^* = 10$), where it represents 12.2% of the total drag for the bare cylinder and 18.8% for the grooved cylinder. Further downstream, it decreases considerably and appears insignificant at $x^* = 40$. The loss in Reynolds shear stresses coincides with the increase in the contribution due to momentum thickness. These results are consistent with observations made by Antonia and Rajagopalan [24]. It is noted that the drag due to Reynolds shear stresses is larger for the grooved cylinder at all downstream locations. The averaged drag coefficient over the various downstream locations tested is 0.958 for the grooved cylinder and 1.025 for the bare cylinder, representing a 6.6% reduction in total drag as a result of surface modification by helical grooves. The present result is in line with that reported by Huang [7], where it is concluded that the helical grooves reduce the inherent drag loading on a bluff structure. The inherent drag reduction from Huang [7] was approximately 25% over the sub-critical Reynolds number region for grooves with a pitch of $6d$, width $0.2d$, and depth $0.15d$. The reason for the improved reduction in drag coefficient may be attributed to the different testing environments used and the dimensions of grooves.

Table 2. Drag coefficients for the bare and grooved cylinders.

Bare Cylinder				Grooved Cylinder			
x^*	I_1	I_2	C_d	x^*	I_1	I_2	C_d
10	0.88	0.122	1.002	10	0.76	0.176	0.936
20	0.96	0.043	1.003	20	0.88	0.055	0.935
40	1.07	0.0001	1.07	40	1	0.0036	1.0036
	Averaged C_d	1.025			Averaged C_d	0.9582	

4.4. Phase-Averaged Vorticity Field and Sectional Streamlines

The phase-averaged sectional streamlines, which are viewed at a reference frame moving with the convection velocity at the vortex centre U_c, are shown in Figure 6, where U_c is the convection velocity at the vortex center. The phase Φ, ranging from -2π to $+2\pi$, can be inferred in terms of a streamwise distance with $\Phi = 2\pi$ corresponding to the vortex wavelength λ. The same scales are used in the Φ- and y^*- directions to avoid distortion of the physical space. The foci and the saddle points are denoted by '+' and '×', respectively. The thick dashed lines indicate the diverging separatrices that pass through the saddles. The typical Kármán structures are identifiable in Figure 6 for both wakes. As evolving downstream, the decay of the spanwise vortices is apparent, as reflected by the gradual shrink in size and the movement away from the centreline. The iso-contours of the phased-averaged spanwise vorticity $\widetilde{\omega}_z \left(= \frac{\partial(\overline{V}+\widetilde{v})}{\partial x} - \frac{\partial(\overline{U}+\widetilde{u})}{\partial y} \right)$ obtained by using Taylor's hypothesis when evaluating the streamwise velocity derivative are shown in Figure 7 for the two cylinder wakes. It can be seen that the vortex centers coincide well with the foci identified from the sectional streamlines (Figure 6). For both wakes at $x^* = 10$, the Kármán

structures are distinctive with staggered positive and negative vortices penetrating to the other side of the wake. Further downstream, the vortices become smaller and expand away from the centerline. It can be seen that the $\widetilde{\omega}_z^*$ contours are consistent with the sectional streamlines. The $\widetilde{\omega}_z^*$ contours at $x^* = 10$ and 20 display the well-known von Kármán vortex streets in both wakes, consistent with that revealed by Figure 6. The vortex streets appear to decay significantly at $x^* = 40$, where the maximum contour values of the coherent vorticities are only about 7% of that at $x^* = 10$. A careful comparison of the bare and grooved cylinder results shows that the grooved cylinder generates a marginally smaller vorticity at $x^* = 10$ and 20. The maximum contour values of $\widetilde{\omega}_z^*$, i.e., 0.8 and 0.25 at $x^* = 10$ and 20 for the grooved cylinder are lower than their counterparts for the bare cylinder, i.e., 0.9 and 0.3, at the corresponding locations, indicating a possible disrupted and weakened vortex shedding for the grooved cylinder. This result coincides with the peak energy on the energy spectra as shown in Figure 4. The difference in the peak energy on the energy spectra is, therefore, attributed to differences in the spanwise vorticity of the wake.
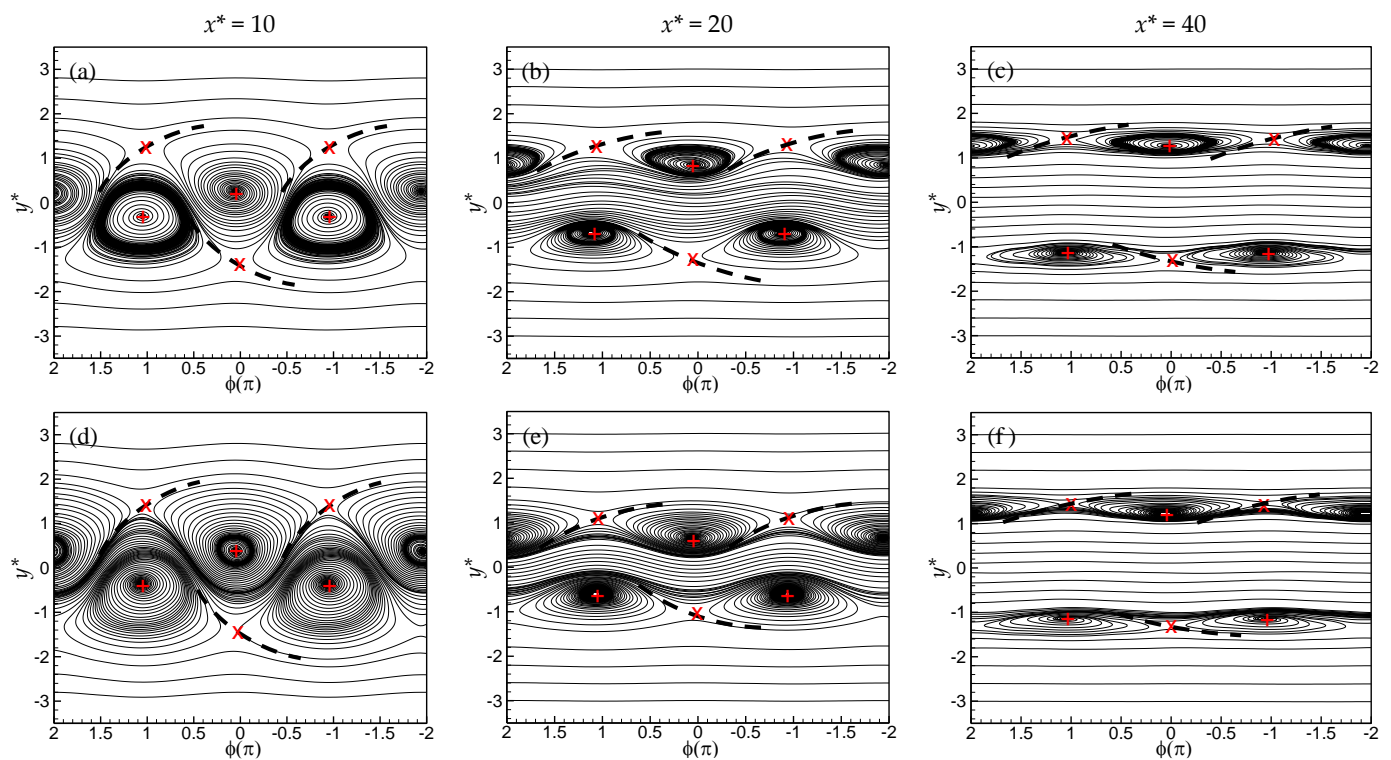
Figure 6. Phase-averaged sectional streamlines for the bare cylinder wake (**a**) at $x^* = 10$; (**b**) at $x^* = 20$; and (**c**) at $x^* = 40$; and the grooved cylinder wake (**d**) at $x^* = 10$; (**e**) at $x^* = 20$; and (**f**) at $x^* = 40$. The plus and the cross represent the foci and the saddle points, respectively. The thick dashed lines indicate the diverging separatrices that pass through the saddles. The flow direction is from left to right.
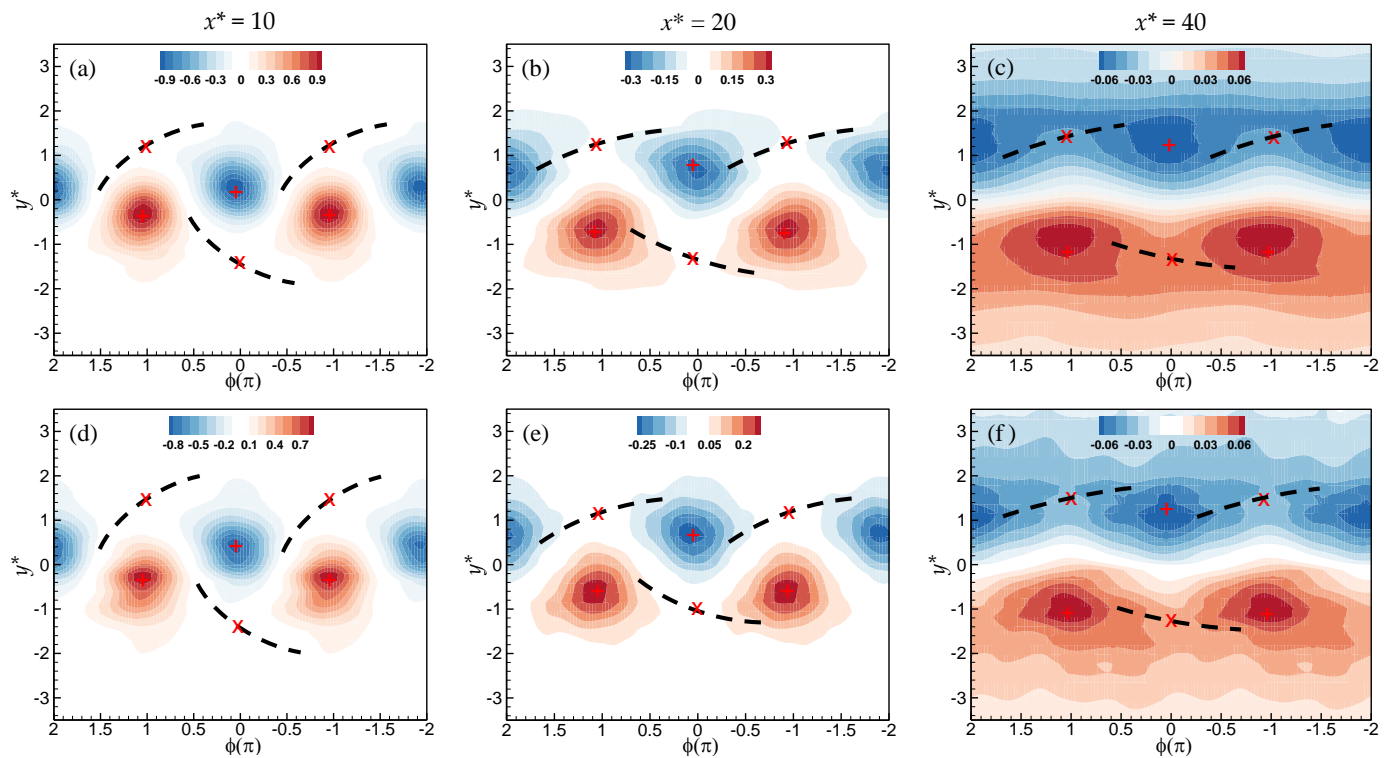
Figure 7. Phase-averaged coherent vorticity, $\widetilde{\omega}_z^*$, for the bare cylinder wake (**a**) at $x^* = 10$, contour interval = 0.1; (**b**) at $x^* = 20$, 0.05; and (**c**) at $x^* = 40$, 0.01; and the grooved cylinder wake (**d**) at $x^* = 10$, 0.1; (**e**) at $x^* = 20$, 0.05; and (**f**) at $x^* = 40$, 0.01. The plus and the cross represent the foci and the saddle points, respectively. The thick dashed lines indicate the diverging separatrices that pass through the saddles. The flow direction is from left to right.

4.5. Phase-Averaged Velocity Fluctuations and Reynolds Shear Stress

Figures 8 and 9 shows the phase-averaged results for the coherent velocity $\widetilde{u}^*$ and $\widetilde{v}^*$. Due to the association with the shear layer vortices, the $\widetilde{u}^*$ contours (Figure 8) display approximate up-down antisymmetry about the vortex center while the $\widetilde{v}^*$ contours (Figure 9) display antisymmetry about $\phi = 0$, which is consistent with that reported by Wang et al. [25] and Zhou et al. [26]. For both wakes, the centers of the $\widetilde{u}^*$ contours are in the vicinity of $y^* = \pm 1$, while those of the $\widetilde{v}^*$ contours are in the vicinity of $y^* = 0$. Furthermore, the maximum contours for both $\widetilde{u}^*$ and $\widetilde{v}^*$ decrease monotonically as evolving downstream due to vortex decay. The maximum contour value (i.e., 0.1) of $\widetilde{u}^*$ at $x^* = 10$ for the grooved cylinder is about 20% lower than that of its counterparts (i.e., 0.12) in the bare cylinder wake, indicating a reduction in vortex shedding strength. However, at the same downstream location of $x^* = 10$ the maximum contours of $\widetilde{v}^*$ in the bare cylinder wake remains at a similar level as the grooved cylinders contradicting the observations by $\widetilde{u}^*$. Moreover, for $x^* = 20$, the discrepancies in the maximum contours of both $\widetilde{u}^*$ and $\widetilde{v}^*$ for the two wakes are indiscernible. Further downstream at $x^* = 40$, the maximum contour values of both $\widetilde{u}^*$ and $\widetilde{v}^*$ in the grooved cylinder wake are higher than those in the bare cylinder wake, suggesting a slower decay rate in the former.
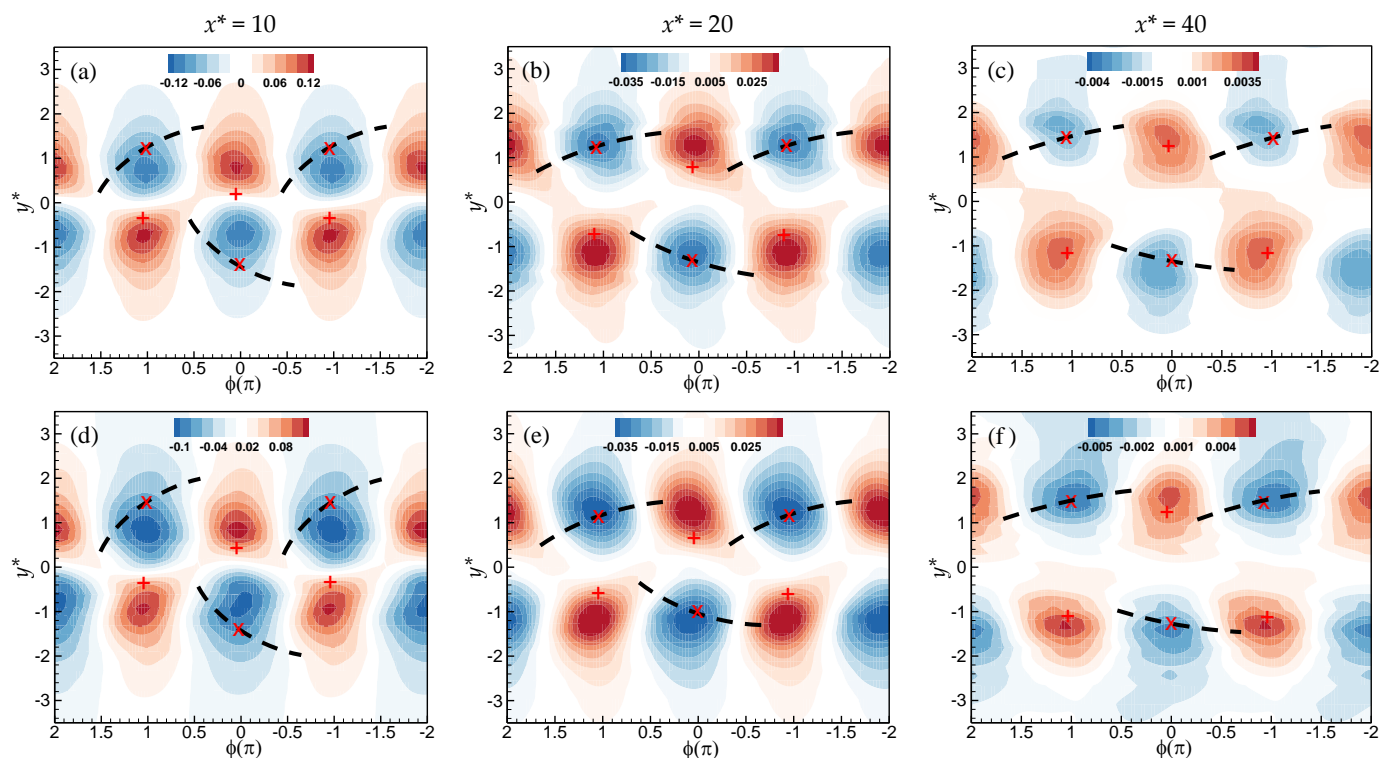
Figure 8. Phase-averaged velocity, $\widetilde{u}^*$, for the bare cylinder wake (**a**) at $x^* = 10$, contour interval = 0.02; (**b**) at $x^* = 20$, 0.005; and (**c**) at $x^* = 40$, 0.0005; and the grooved cylinder wake (**d**) at $x^* = 10$, 0.02; (**e**) at $x^* = 20$, 0.005; and (**f**) at $x^* = 40$, 0.001. The plus and the cross represent the foci and the saddle points, respectively. The thick dashed lines indicate the diverging separatrices that pass through the saddles. The flow direction is from left to right.

Figure 10 shows the contours of the coherent Reynolds shear stress $\widetilde{u}^*\widetilde{v}^*$ for both wakes. The grooved cylinder wake displays a well-established clover-leaf pattern about the vortex center, as reported previously [27]. The maximum coherent contours of $\widetilde{u}^*\widetilde{v}^*$ reveal a monotonic decreasing trend with the increase of x^* in the two wakes, which is the same as those shown in Figures 8 and 9. The maximum contour value of $\widetilde{u}^*\widetilde{v}^*$, i.e., 0.012, at $x^* = 10$ for the grooved cylinder wake is smaller than its counterpart for the bare cylinder wake, i.e., 0.016, indicating a weakened vortex shedding for the grooved cylinder in the near wake. For $x^* = 20$, the maximum contour values for both grooved cylinder and bare cylinder are comparable. These results are in agreement with that revealed by the coherent spanwise vorticity contours (Figure 7). However, for the grooved cylinder wake at $x^* = 40$, the maximum contour values of $\widetilde{v}^*$ (i.e., 0.012 in Figure 9) and the maximum contour values of $\widetilde{u}^*\widetilde{v}^*$ (i.e., 3×10^{-5} in Figure 10) are both higher than their counterparts for the bare cylinder wake, i.e., 0.007 of $\widetilde{v}^*$ in Figure 9 and 2×10^{-5} of $\widetilde{u}^*\widetilde{v}^*$ in Figure 10, respectively. This observation seems to suggest that the vortices in the grooved cylinder wake have less vigorous interaction across the wake centerline, resulting in a slower decay rate of the vortices in the streamwise direction. A similar result was also found in screen cylinder wakes [27], where vortices generated from the screen cylinder decay at a much slower rate compared with those in the bare cylinder wake due to weak interaction of the vortices across the wake centerline.
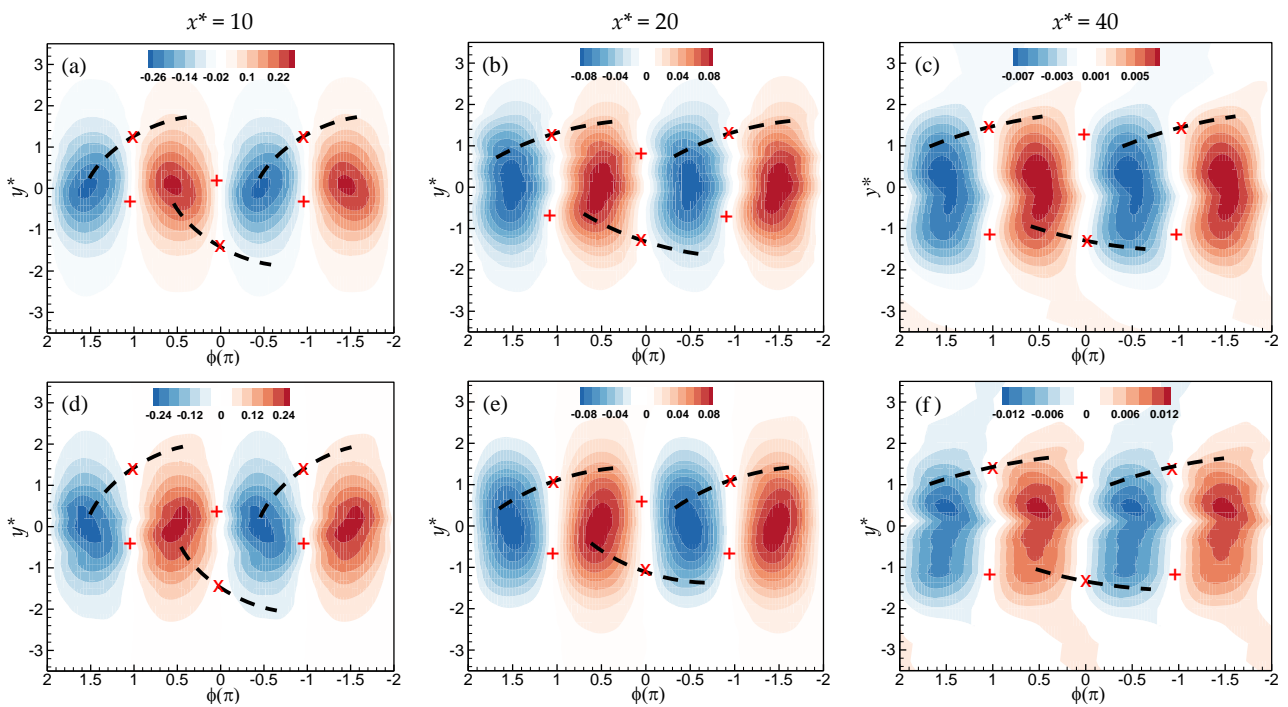
Figure 9. Phase-averaged velocity, $\widetilde{v}^*$, for the bare cylinder wake (**a**) at $x^* = 10$, contour interval = 0.04; (**b**) at $x^* = 20$, 0.01; and (**c**) at $x^* = 40$, 0.001; and the grooved cylinder wake (**d**) at $x^* = 10$, 0.04; (**e**) at $x^* = 20$, 0.01; and (**f**) at $x^* = 40$, 0.002. The plus and the cross represent the foci and the saddle points, respectively. The thick dashed lines indicate the diverging separatrices that pass through the saddles. The flow direction is from left to right.
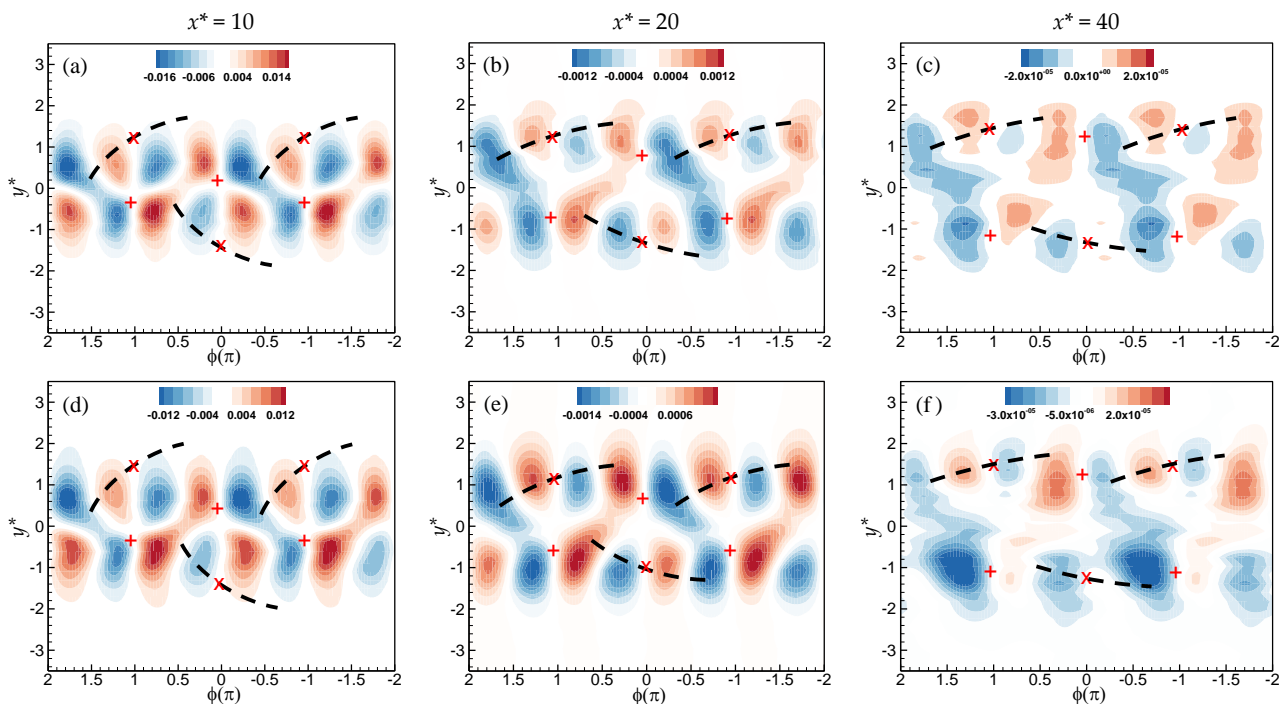
Figure 10. Phase-averaged Reynolds shear stress, $\widetilde{u}^*\widetilde{v}^*$, for the bare cylinder wake (**a**) at $x^* = 10$, contour interval = 0.002; (**b**) at $x^* = 20$, 0.0002; and (**c**) at $x^* = 40$, 0.00001; and the grooved cylinder wake (**d**) at $x^* = 10$, 0.002; (**e**) at $x^* = 20$, 0.0002; and (**f**) at $x^* = 40$, 0.000005. The plus and the cross represent the foci and the saddle points, respectively. The thick dashed lines indicate the diverging separatrices that pass through the saddles. The flow direction is from left to right.

4.6. Coherent and Incoherent Contributions to Reynolds Stresses

After the coherent components $\widetilde{u}^*$, $\widetilde{v}^*$, and $\widetilde{u}^*\widetilde{v}^*$ fluctuations are extracted using the phase-averaged technique, the coherent contributions to the Reynolds stresses can be evaluated in terms of the structural average (Equation (7)). Figures 11 and 12 show the coherent and incoherent contributions to the time-averaged Reynolds stresses for both wakes. The results for the bare cylinder wake (Figure 11) are in good agreement with those reported previously [25], thus providing a validation of the present measurement. The time-averaged Reynolds stresses are quite symmetrical about $y^* = 0$ for both wakes. At $x^* = 10$, the maximum values of $\overline{u^{*2}}$, $\overline{v^{*2}}$, and $\overline{u^*v^*}$ in the grooved cylinder wake are 0.025, 0.007, and 0.004, and, thus, 10%, 14.3%, and 25% lower than their counterparts of 0.0275, 0.008, and 0.005 in the bare cylinder wake, respectively, indicating that the grooves decrease the intensity of coherent vortices. It is noted that $\overline{\widetilde{u}^{*2}}$ shows a twin-peak distribution in both wakes at $x^* = 10$. This is consistent with the contour patterns shown in Figure 8. At $y^* = \pm 0.75$, the coherent component is approximately 35% of the incoherent one. It is apparent that the coherent structures contribute more significantly to the v than the u components at $x^* = 10$ for both wakes, where its contribution is 62.5% by integrating the area under the distributions, indicating a greater sensitivity to large, organized structures in the lateral direction. These results coincide with those shown in Figures 8 and 9, where the phase-averaged maximum contour values of $\widetilde{v}^*$ is 0.24 for the grooved cylinder while the maximum values of $\widetilde{u}^*$ is only 0.1. Further downstream, the results for the grooved cylinder are almost identical to those of the bare cylinder in terms of coherent and incoherent contributions to velocity variance, where there exists significant decay in both the coherent and incoherent components.
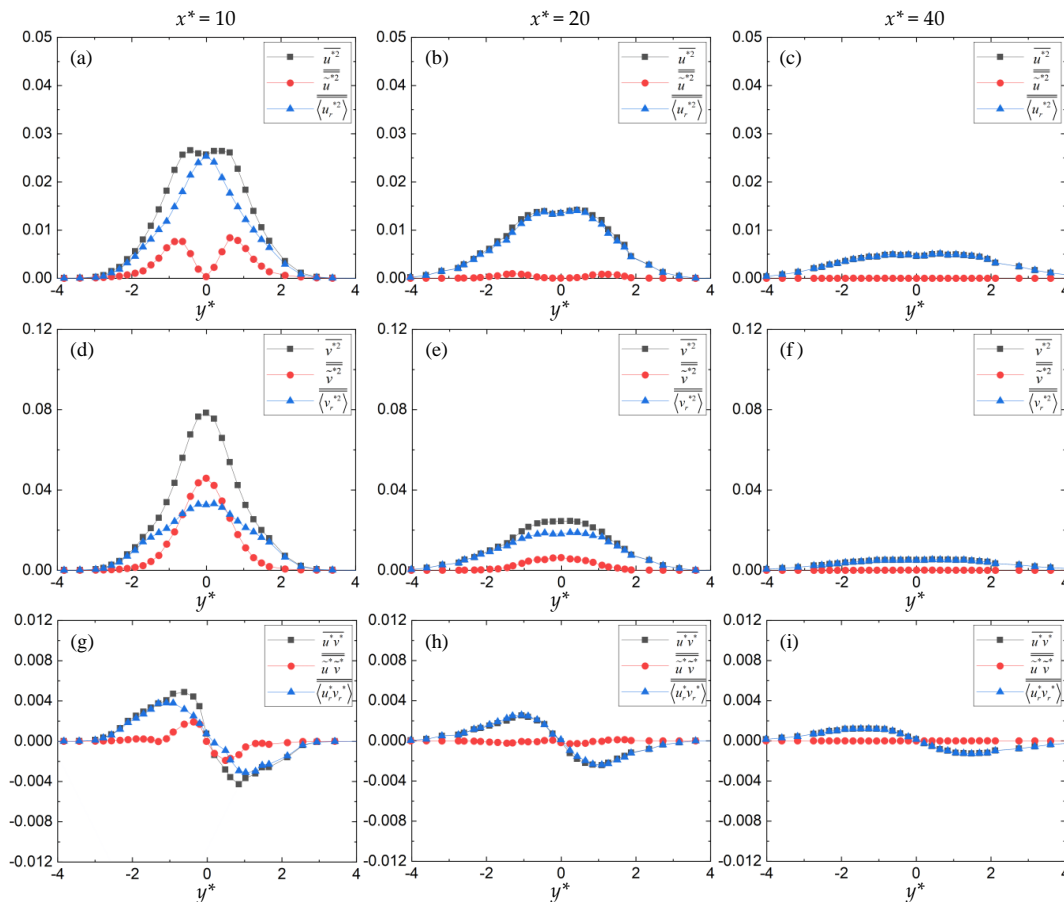
Figure 11. Coherent (○) and incoherent (Δ) contributions to the time-averaged (●) Reynold stresses for the bare cylinder wake. (**a**–**c**) Reynolds normal stress *uu*; (**d**–**f**) Reynolds normal stress *vv*; and (**g**–**i**) Reynolds shear stress *uv*.
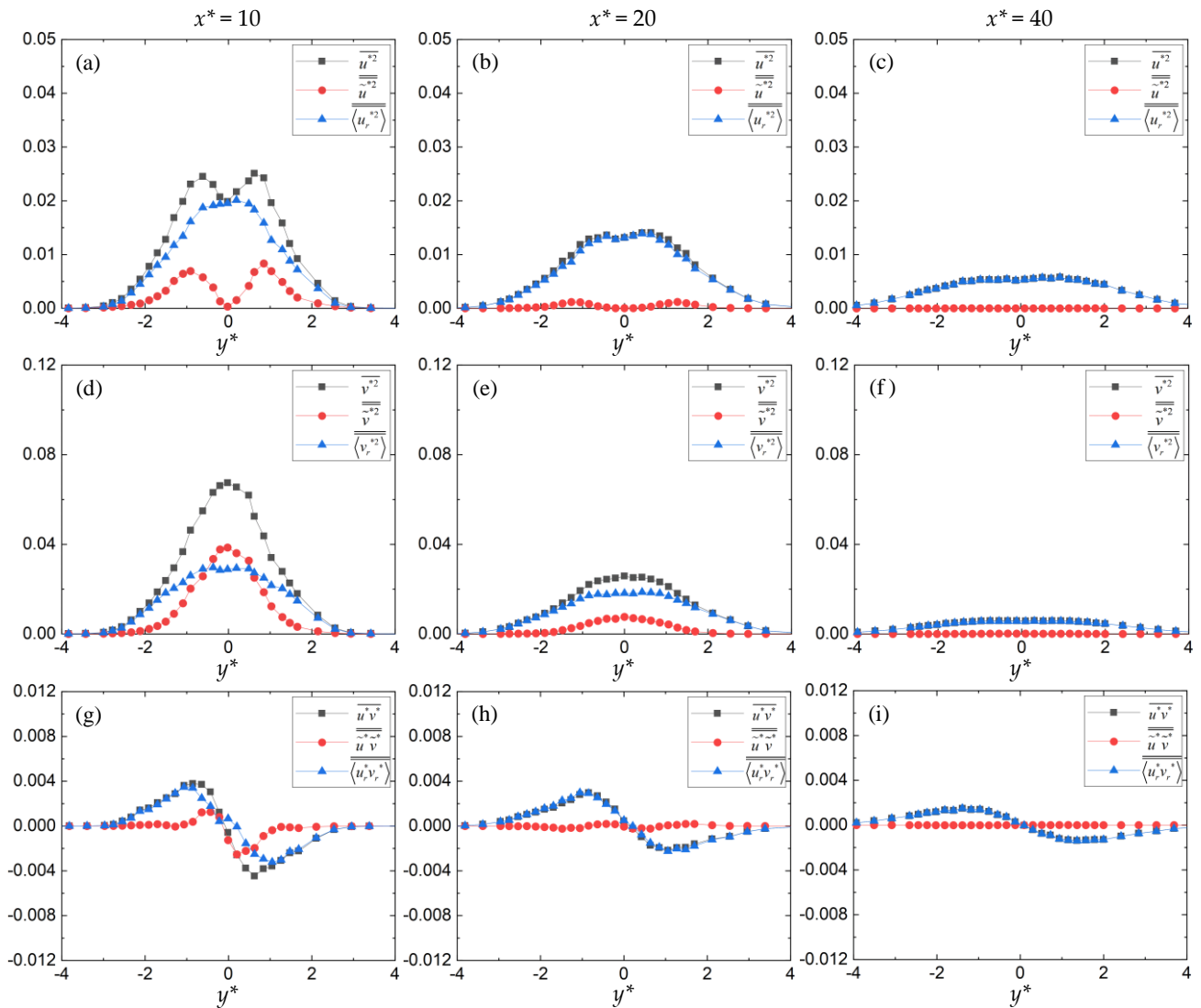
Figure 12. Coherent (○) and incoherent (Δ) contributions to the time-averaged (●) Reynold stresses for the grooved cylinder wake. (**a**–**c**) Reynolds normal stress *uu*; (**d**–**f**) Reynolds normal stress *vv*; and (**g**–**i**) Reynolds shear stress *uv*.

The streamwise variation of the coherent contribution can also be quantified by examining the variation of the ratio $\widetilde{\bar{\bar{\beta}}\widetilde{\gamma}}/\overline{\beta\gamma}$ in the streamwise direction, where β and γ represent u and/or v. Since this ratio varies with y^*, an averaged contribution $\left(\widetilde{\bar{\bar{\beta}}\widetilde{\gamma}}/\overline{\beta\gamma}\right)_m$ from the vortical structures across the wake at a given streamwise location is defined as:

$$\left(\widetilde{\bar{\bar{\beta}}\widetilde{\gamma}}/\overline{\beta\gamma}\right)_m = \int_{-\infty}^{\infty}\left|\widetilde{\bar{\bar{\beta}}\widetilde{\gamma}}\right|dy^* / \int_{-\infty}^{\infty}\left|\overline{\beta\gamma}\right|dy^* \tag{12}$$

where the subscript m denotes the averaged value across the wake. The calculated values of $\left(\widetilde{\bar{\bar{\beta}}\widetilde{\gamma}}/\overline{\beta\gamma}\right)_m$ are given in Table 3. The values are internally consistent with the results for $\overline{\beta\gamma}$, $\widetilde{\bar{\bar{\beta}}\widetilde{\gamma}}$ and $\left\langle \overline{\beta_r\gamma_r} \right\rangle$ in Figures 11 and 12. It can be seen that at $x^* = 10$, $\left(\widetilde{\bar{\bar{u}}^2}/\overline{u^2}\right)_m$, $\left(\widetilde{\bar{\bar{v}}^2}/\overline{v^2}\right)_m$ and $\left(\widetilde{\bar{\bar{u}}\widetilde{v}}/\overline{uv}\right)_m$ for the grooved cylinder wake are about 12%, 6.8%, and 15% lower than their counterparts in the bare cylinder wake. It is, therefore, obvious that the vortices in the

bare cylinder wake contain more energy than that in the grooved cylinder wake. Further downstream, the trend is the opposite, i.e., the values in the bare cylinder wake are smaller than those in the grooved cylinder wake, indicating a faster decay of the coherent vortices in the former wake. This is more evidenced in terms of the ratios between the coherent and incoherent components, $\left(\overline{\widetilde{u}^2}/\overline{u_r^2}\right)_m$ and $\left(\overline{\widetilde{v}^2}/\overline{v_r^2}\right)_m$ (Table 3), where a higher level of the coherent contribution indicates a stronger coherent vortex in the wake. It is noted that the coherent contribution decreases significantly in the streamwise direction, indicating the weaker vortices with the increase of x^*. For instance, from $x^* = 10$, $\left(\overline{\widetilde{v}^2}/\overline{v^2}\right)_m$ drops by 49% and 97% at $x^* = 20$ and 40, respectively, in the grooved cylinder wake.

Table 3. Maximum values of the Reynolds stresses and averaged contributions from the coherent motion to the Reynolds stresses and the ratios of the coherent to random motions.

	Bare Cylinder		
x^*	10	20	40
$\left\|\overline{u^{*2}}_{max}\right\|$	0.027	0.015	0.005
$\left\|\overline{v^{*2}}_{max}\right\|$	0.008	0.025	0.005
$\left\|\overline{u^*v^*}_{max}\right\|$	0.005	0.003	0.001
$\left(\overline{\widetilde{u}^2}/\overline{u^2}\right)_m$ (%)	25	5	0.2
$\left(\overline{\widetilde{v}^2}/\overline{v^2}\right)_m$ (%)	44	16	0.9
$\left(\overline{\widetilde{u}\widetilde{v}}/\overline{uv}\right)_m$ (%)	27	7	0.3
$\left(\overline{\widetilde{u}^2}/\overline{u_r^2}\right)_m$	0.33	0.05	0.002
$\left(\overline{\widetilde{v}^2}/\overline{v_r^2}\right)_m$	0.79	0.19	0.009
$\left(\overline{\widetilde{u}\widetilde{v}}/\overline{u_r v_r}\right)_m$	0.37	0.08	0.003
	Grooved Cylinder		
x^*	10	20	40
$\left\|\overline{u^{*2}}_{max}\right\|$	0.025	0.014	0.006
$\left\|\overline{v^{*2}}_{max}\right\|$	0.007	0.026	0.006
$\left\|\overline{u^*v^*}_{max}\right\|$	0.004	0.003	0.002
$\left(\overline{\widetilde{u}^2}/\overline{u^2}\right)_m$ (%)	22	7	0.3
$\left(\overline{\widetilde{v}^2}/\overline{v^2}\right)_m$ (%)	41	21	1.2
$\left(\overline{\widetilde{u}\widetilde{v}}/\overline{uv}\right)_m$ (%)	23	9	0.5
$\left(\overline{\widetilde{u}^2}/\overline{u_r^2}\right)_m$	0.28	0.08	0.003
$\left(\overline{\widetilde{v}^2}/\overline{v_r^2}\right)_m$	0.69	0.27	0.012
$\left(\overline{\widetilde{u}\widetilde{v}}/\overline{u_r v_r}\right)_m$	0.30	0.10	0.005

5. Conclusions

The wake characteristics of a grooved cylinder have not been documented extensively in the literature. In the present study, the effectiveness of three strand helical grooves with a pitch of 7.5d, a width of 0.2d, and a depth of 0.12d on the suppression of VIV is examined in a wind tunnel over reduced velocity V_r in the range of 3–11. It is found that the helical grooves are effective in suppressing VIV with the peak amplitude reduction of approximately 36%. In addition, the lock-on region is also reduced. The spectral analysis shows that regular vortex shedding from the grooved cylinder is also apparent. The peak energy at a downstream location of $x^* = 10$ is higher in the bare cylinder wake than that in the grooved counterpart, indicating that the grooves may help enhance the three-dimensionality of the flow and consequently decrease the intensity of vortex shedding. This result is supported by the cross-correlation coefficient of the transverse velocity components, which reveals that the vortical structures in the wake of the bare cylinder are about 30% larger than that in the grooved cylinder wake at $x^* = 10$. The 6.6% lower drag coefficient of the grooved cylinder than the bare cylinder is in line with that reported by Huang [7], where it is concluded that the helical grooves reduce the inherent drag loading on the cylinder. To further explore the fundamental mechanism of the grooves in reducing VIV response, the vortex structures and turbulent characteristics of a circular cylinder wake, with and without helical grooves, are also examined using a phase-averaged method at a Reynolds number $Re = 3500$ over a streamwise range of $x^* = 10$–40 in a wind tunnel. Phase-averaged analysis shows that the grooved cylinder generates a marginally smaller coherent spanwise vorticity at $x^* = 10$ and 20 than that of a bare cylinder, indicating a possible disrupted and weakened vortex shedding for the grooved cylinder wake. The maximum phase-averaged contour values of the Reynolds stresses at $x^* = 10$ for the grooved cylinder are smaller than their counterparts for the bare cylinder, further supporting a weakened vortex shedding in the near wake of a grooved cylinder.

Author Contributions: Conceptualization, T.Z.; methodology, T.Z. and Z.H.; software, C.S.; validation, C.S.; formal analysis, C.S., Z.H. and Y.L.; investigation, Z.H.; resources, T.Z.; data curation, T.Z.; writing—original draft preparation, Z.H. and C.S.; writing—review and editing, Z.H., C.S., Y.L., K.B. and T.Z.; funding acquisition, T.Z. and K.B. All authors have read and agreed to the published version of the manuscript.

Data Availability Statement: The data that support the findings of this study are available from the corresponding author upon reasonable request.

References

1. Sumer, B.M.; Fredsøe, J. *Hydrodynamics around Cylindrical Structures*; World Scientific: Singapore, 1997.
2. Zdravkovich, M.M. Review and classification of various aerodynamic and hydrodynamic means for suppressing vortex shedding. *J. Wind Eng. Ind. Aerodyn.* **1981**, *7*, 145–189. [CrossRef]
3. Rabiee, A.; Esmaeili, M. Simultaneous vortex- and wake-induced vibration suppression of tandem-arranged circular cylinders using active feedback control system. *J. Sound Vib.* **2019**, *469*, 115131. [CrossRef]
4. Wang, J.; Lin, D.K.; Lin, K. A review on flow-induced vibration of offshore circular cylinders. *J. Hydrodyn.* **2020**, *32*, 415–440. [CrossRef]
5. Ma, Y.; Xu, W.; Ai, H.; Wang, Y.; Jia, K. The effect of time-varying axial tension on VIV suppression for a flexible cylinder attached with helical strakes. *Ocean. Eng.* **2021**, *241*, 109981. [CrossRef]
6. Zhou, T.; Mohd Razal, S.F.; Hao, Z.; Cheng, L. On the study of vortex-induced vibration of a cylinder with helical strakes. *J. Fluids Struct.* **2011**, *27*, 903–917. [CrossRef]
7. Huang, S. VIV suppression of a two-degree-of-freedom circular cylinder and drag reduction of a fixed circular cylinder by the use of helical grooves. *J. Fluids Struct.* **2011**, *27*, 1124–1133. [CrossRef]
8. Ishihara, T.; Li, T. Numerical study on suppression of vortex-induced vibration of circular cylinder by helical wires. *J. Wind Eng. Ind. Aerodyn.* **2020**, *197*, 104081. [CrossRef]
9. Law, Y.Z.; Jaiman, R.K. Passive control of vortex-induced vibration by spanwise grooves. *J. Fluids Struct.* **2018**, *83*, 1–26. [CrossRef]

10. Zhou, B.; Wang, X.; Guo, W.; Zheng, J.; Tan, S.K. Experimental measurements of the drag force and the near-wake flow patterns of a longitudinally grooved cylinder. *J. Wind Eng. Ind. Aerodyn.* **2015**, *145*, 30–41. [CrossRef]
11. Sun, C.; Azmi, A.M.; Hao, Z.; Zhu, H.; Zhou, T. Suppression of vortex shedding and vortex-induced vibration of a circular cylinder using screen shrouds. *Appl. Ocean. Res.* **2022**, *122*, 103146. [CrossRef]
12. Hussain, A.F. Coherent structures and turbulence. *J. Fluid Mech.* **1986**, *173*, 303–356. [CrossRef]
13. Kiya, M.; Matsumura, M. Incoherent turbulence in the near wake of a normal plate. *J. Fluid Mech.* **1988**, *190*, 343–356. [CrossRef]
14. Zhou, Y.; Zhang, H.; Yiu, M. The turbulent wake of two side-by-side circular cylinders. *J. Fluid Mech.* **2002**, *458*, 303–332. [CrossRef]
15. Matsumura, M.; Antonia, R.A. Momentum and heat-transport in the turbulent intermediate wake of a circular-cylinder. *J. Fluid Mech.* **1993**, *250*, 651–668. [CrossRef]
16. Zhou, T.; Zhou, Y.; Chua, L.P.; Yiu, M.W. Three-dimensional vorticity in turbulent cylinder wake. *Exp. Fluids* **2003**, *35*, 459–471. [CrossRef]
17. Hussain, A.K.M.F.; Reynolds, W.C. The mechanics of an organized wave in turbulent shear flow. *J. Fluid Mech.* **1970**, *41*, 241–258. [CrossRef]
18. Franzini, G.R.; Fujarra, A.L.C.; Meneghini, J.R.; Korkischko, I.; Franciss, R. Experimental investigation of vortex-induced vibration on rigid, smooth and inclined cylinders. *J. Fluids Struct.* **2009**, *25*, 742–750. [CrossRef]
19. Hover, F.S.; Tvedt, H.; Triantafyllou, M.S. Vortex-induced vibrations of a cylinder with tripping wires. *J. Fluid Mech.* **2001**, *448*, 175–195. [CrossRef]
20. Feng, C.C. The Measurement of Vortex Induced Effects in Flow Past Stationary and Oscillating Circular and D-Section Cylinders. Master's Thesis, University of British Columbia, Vancouver, BC, Canada, 1968.
21. Norberg, C. Fluctuating lift on a circular cylinder: Review and new measurements. *J. Fluids Struct.* **2003**, *17*, 57–96. [CrossRef]
22. Bearman, P.; Brankovic, M. Experimental studies of passive control of vortex-induced vibration. *Eur. J. Mech. Fluids* **2004**, *23*, 9–15. [CrossRef]
23. Blevins, R.D. *Flow Induced Vibrations*, 2nd ed.; Krieger: Malabar, FL, USA, 1990.
24. Antonia, R.A.; Rajagopalan, S. Determination of drag of a circular cylinder. *AIAA J.* **1990**, *28*, 1833–1834. [CrossRef]
25. Wang, H.F.; Razali, S.F.M.; Zhou, T.M.; Zhou, Y.; Cheng, L. Streamwise evolution of an inclined cylinder wake. *Exp. Fluids* **2011**, *51*, 553–570. [CrossRef]
26. Zhou, T.; Wang, H.; Razali, F.M.; Zhou, Y.; Cheng, L. Three-dimensional vorticity measurements in the wake of a yawed circular cylinder. *Phys. Fluids* **2010**, *22*, 015108. [CrossRef]
27. Sun, C.; Azmi, A.M.; Leontini, J.; Zhu, H.; Zhou, T. Experimental study on the development of wake vortices behind screen cylinders. *Phys. Fluids* **2021**, *33*, 085133. [CrossRef]